Chapter 5

Noise Model for a Time-Domain Breast Imaging System

A detailed system characterization of the Time-Domain Breast Imaging System is presented in Chapter 6. The motivation for the characterization effort was to provide greater understanding of how the system could be configured to result in optimal clinical performance. One of the best methods for assessing system-level performance is through an analysis of the signal-to-noise ratio (SNR). Attempts to explain the results of the SNR analysis proved difficult in the absence of a noise theory. This prompted a review of the literature for ICCD systems. No complete or even semi-complete noise theory was found in the literature for ICCD systems [1,2]. This presented the opportunity to develop a comprehensive noise theory that not only covers the ICCD, but incorporates all recognized contributions to the noise for our system architecture. This theory is the most compete ever developed, based on a review of the literature, and provides the foundation for understanding both the SNR behavior of the Time-Domain Optical Breast Imaging System and insight as to methods for improving overall system performance and thus, clinical performance.

5.1 Noise Model for an Image Intensified CCD Camera System and Time-Domain Breast Imaging System

The following discussion comprises the derivation of a noise model for an image intensified charge coupled device camera (ICCD) as part of the Time-Domain Optical

Breast Imaging System. The motivation for this noise model was to provide insight into the noise behavior of an ICCD used in conjunction with a Ti:Sapphire laser source and a fiber optic probe. This insight will be used to determine the best operating parameters for the system to enable image optimization within the context of Time-Domain DOT clinical breast imaging.

The ICCD is a complex system with many sources of noise. Generally, the noise can be segmented into that due to the intensifier and that due to the CCD. The primary sources of noise for the intensifier are photon (shot) noise with contributions from the signal and background incident on the photocathode, dark noise in the form of thermionic emission of photoelectrons from the photocathode, and noise due to the gain process through the microchannels. The primary sources of noise for the CCD camera are photon noise, dark noise and readout noise.

5.1.1 Assumptions

The focus of this discussion will initially be on the ICCD only. A non-thermal source is assumed, such that the randomness in the arrival rate of the photons obeys Poisson statistics (that is, the Bose-Einstein nature of a thermal radiation field is not considered) [3]. The effects on the system noise of pulse-to-pulse amplitude fluctuations in the laser, intensity fluctuations due to mirror dithering in the Multiplexer, and fluctuations in microchannel plate gain voltage will be addressed in Section 5.1.11.

5.1.2 Basic Operating Principles of an ICCD Camera

The primary components of an ICCD camera are shown in Figure 5.1. The picture depicts a proximity-focused image intensifier, for which the anode of the microchannel

plate (MCP) is placed in close enough proximity to the phosphor electrode as to achieve sufficient localization of the light emitted by the phosphor. A photon incident through the input window strikes the photocathode causing the release of a photoelectron by the photoelectric effect. In its "on" state, the photoelectron is accelerated toward the MCP by

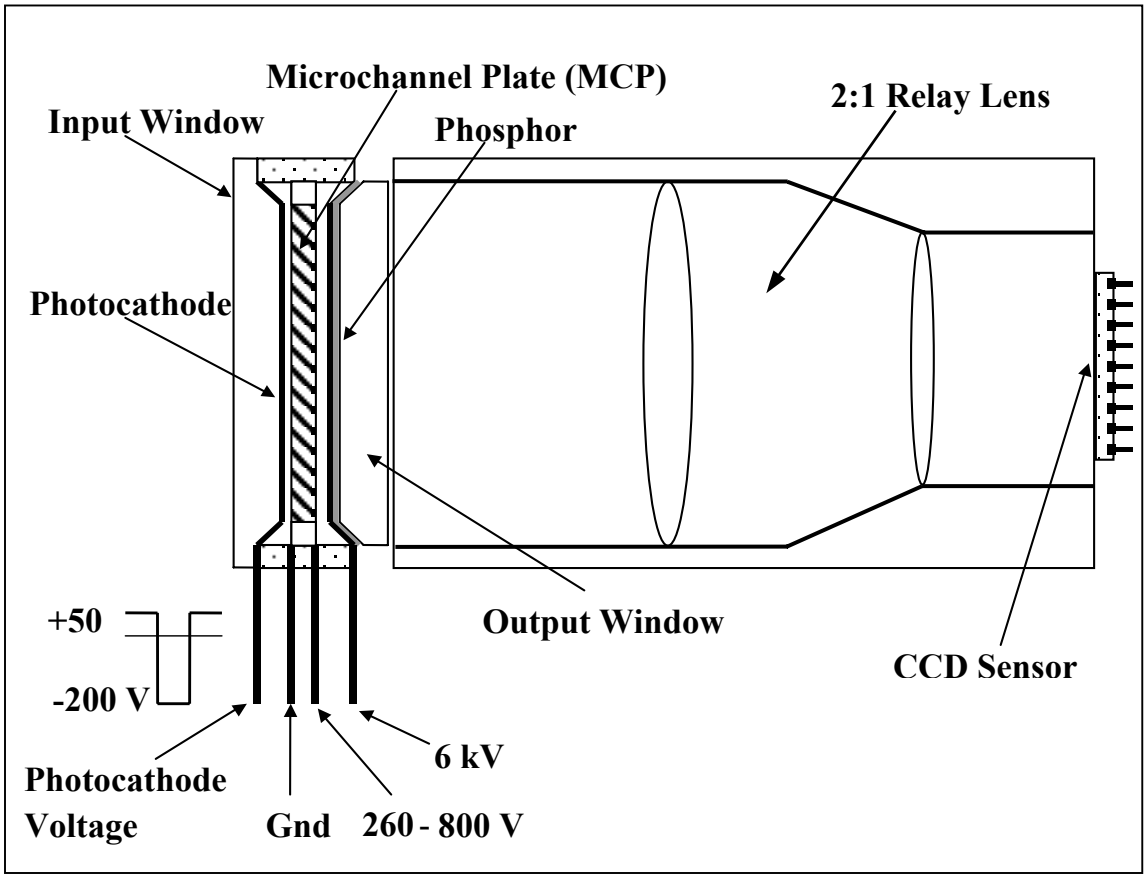

Figure 5.1. The basic functionality of the ICCD is shown above in cross section. Photons enter from the left striking the photocathode, thereby generating a primary photoelectron that is accelerated by a potential of 200 Volts toward the input face of the microchannel plate. The photoelectron strikes the wall of one of the many channels in the MCP where it causes the release of secondary emitted electrons. This process repeats as the cascade of electrons is accelerated down the channel toward the exit face. The electron cloud is then accelerated toward the phosphor layer by a large potential. Light emitted by the phosphor is then imaged by the relay lens system onto the CCD.

a potential on the order of -200 Volts. The photoelectron then strikes the inner wall of one of the closely-packed hollow channels in the glass-substrate MCP as shown in Figure 5.2. The process of electron amplification in a microchannel is analogous to electron

amplification in a photomultiplier tube (PMT) for which a series of metal contacts called dynodes are covered with a secondary emission material to produce a cascade of electrons at the output in response to a single primary photoelectron by the process of secondary emission. A potential exists between successive dynodes acting to accelerate the growing cascade of electrons as they cascade toward the anode. In the case of the microchannel, there are no discrete dynodes. There is, however, a potential between the end-faces of the MCP. This causes the low energy electrons emitted by the process of secondary emission to accelerate through a parabolic path down the channel toward the positive potential. Successive cascades of electrons collide with the walls as the process of electron amplification progresses down the microchannel. Thus, the process can be modeled in a way analogous to that used to describe the classic PMT dynode chain. The cascade of secondary electrons exiting the MCP is then accelerated by a high potential on the order of 6 kV toward a phosphor layer. For every electron incident on the phosphor, approximately 200 green photons are produced. The relay lens system then captures the small fraction of photons within its angular field of view and maps them onto the CCD sensor. A large fraction of these photons is then converted into electrons and is stored in a well for a specific integration period. A shift register then consecutively shifts the charge out of the device where it is converted from an analog charge to a digital signal read out as counts with a dynamic range of 4096 counts (12 bits).

The potential on the photocathode can be modulated between a positive potential (relative to the entrance face of the MCP, which is at ground potential) of approximately +50 Volts and a negative potential on the order of –200 Volts. It operates with a time constant that allows for signal gating up to about 1 GHz (with a maximum duty cycle of

50%) according to the manufacturer's specification (LaVision). In the positive potential state, the photoelectrons are repelled by the electric field in a direction opposite that of

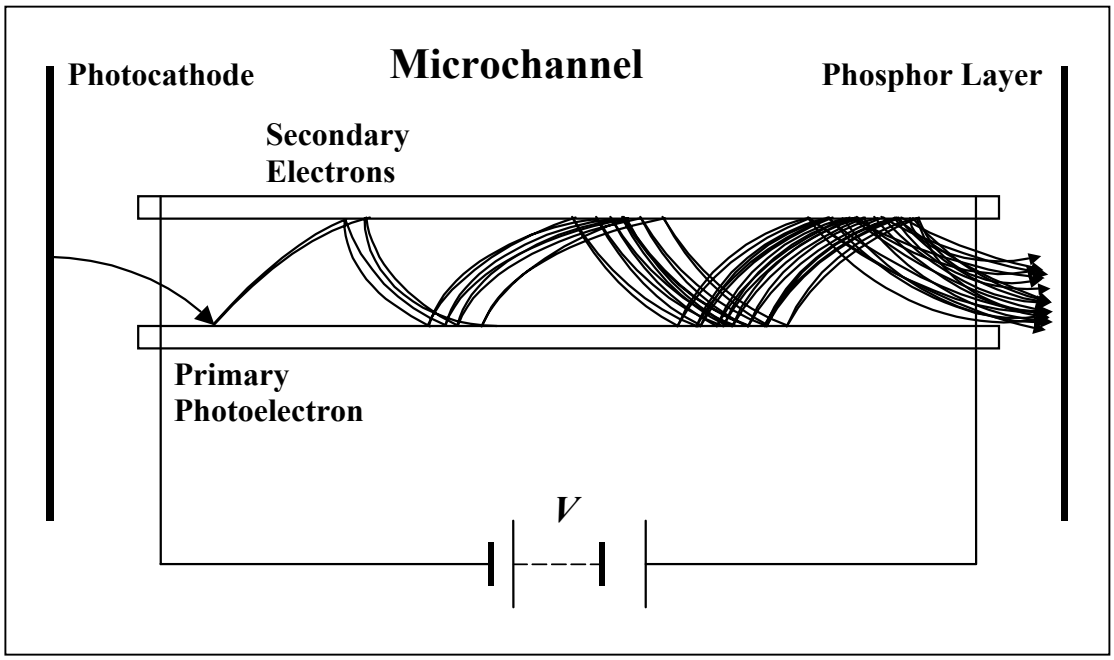

Figure 5.2. A single microchannel of a MCP is shown. A photoelectron is emitted by the photocathode and strikes the wall of the microchannel tube. One or more secondary electrons will be emitted, given a sufficiently high voltage *V* across the faces of the microchannel and a sufficiently energetic photoelectron. This secondary emission amplification process causes a cascade of electrons to strike the phosphor, which then emits green light, which is subsequently imaged onto the CCD.

the MCP and thus there is no signal to amplify. When the gate signal is at a potential of –200 Volts, the electric field accelerates photoelectrons toward the MCP and thus an amplified signal results. Thus, the ICCD can be gated in synchronization with the 80 MHz pulse-rate Ti:Sapphire laser output of the breast imaging system. To rebuild a complete temporal point spread function (TPSF) the system must measure the relative signal over a range of time gate delays. The CCD camera does not have a sufficiently fast response time to record individual gate events. Therefore, it must be used as an integrator. A typical integration time might be on the order of 100 msec, which would

contain approximately 8 million individual laser pulses and ICCD gate cycles. There is some small, but finite probability (<<1) that a photon will strike the photocathode during the gate period and result in a contribution to the total charge in the CCD well, within the CCD's integration period. This is an overly simplistic view of the process, but provides the framework with which to describe the various noise components.

A material is vapor deposited on the surface of the hollow channels of the MCP, characterized by a secondary emission ratio δ defined as the ratio of the average number of secondary electrons leaving the surface to the number of primary electrons incident on the surface [3-5]. The ratio depends nearly linearly on the kinetic energy of the primary electron. The kinetic energy of the primary electron depends on the electric field strength, which is a function of the potential between the successive collision points along the channel and consequently, a function of the potential between the electrodes immediately inside the faces of the MCP. The total gain of the microchannel plate is given by

$$G_{MCP} = \delta(V)^{N_{eff}} \qquad (5.1)$$

where the dependence has been noted of the secondary emission ratio on the voltage *V,* and the effective number of secondary emission zones or effective "dynodes" has been referred to as N_{eff}. Typical values of δ range from somewhat over 1 to the order of 10 or more, depending on material and voltage. The device used in the breast imaging system had a maximum gain on the order of 100 counts per photoelectron. The electron gain was much higher to account for low quantum efficiencies, particularly in the near infrared, and phosphor collection efficiency.

5.1.3 Intensifier Photocathode and the Photoelectric Effect

The photoelectric effect is defined as the emission of electrons from the surface of a material through the absorption of incident photons. It was first discovered by Hertz and a few years later explained by Albert Einstein that if a beam of monochromatic light of frequency ν falls onto a metal surface, electrons are emitted from the surface with a kinetic energy given by

$$KE = h\nu - \phi \tag{5.2}$$

where the energy of the incident photon is the product of the photon frequency and Plank's constant *h,* and ϕ is a constant material property know as the work function [3,5]. The work function can be thought of as the binding energy of the electron to the metal.

Figure 5.3 A shows the electronic energy-level structure of a metal. Electrons obey Fermi-Dirac statistics, so no more than one electron can occupy a given quantum mechanical state of the system [3]. Thus at a temperature of absolute zero, all the single-electron states will be occupied whose energies range from the minimum allowed value, which is taken as zero on this energy scale, to an energy value referred to as the Fermi energy. The vacuum level refers to an electron located infinitely far from the surface of the metal, having zero kinetic energy. The minimum energy required to remove an electron from the surface is the difference in energy between the vacuum and Fermi levels, which is defined as the work function ϕ. Typical work functions of metals are in the several electron volt range, with the lowest value of 2.0 electron volts for elemental Cesium (Cs), corresponding to 620 nm cut-off. Thus, metal photocathodes are not useful in the near infrared spectrum of the physiological window between about 650 and 1000 nm.

Figure 5.3 B depicts the electronic energy-level structure of a typical semiconductor, which is the basis of the most common photocathodes in use today, such as the popular S20 series used in the TD breast imaging system. The photoelectric effect also takes

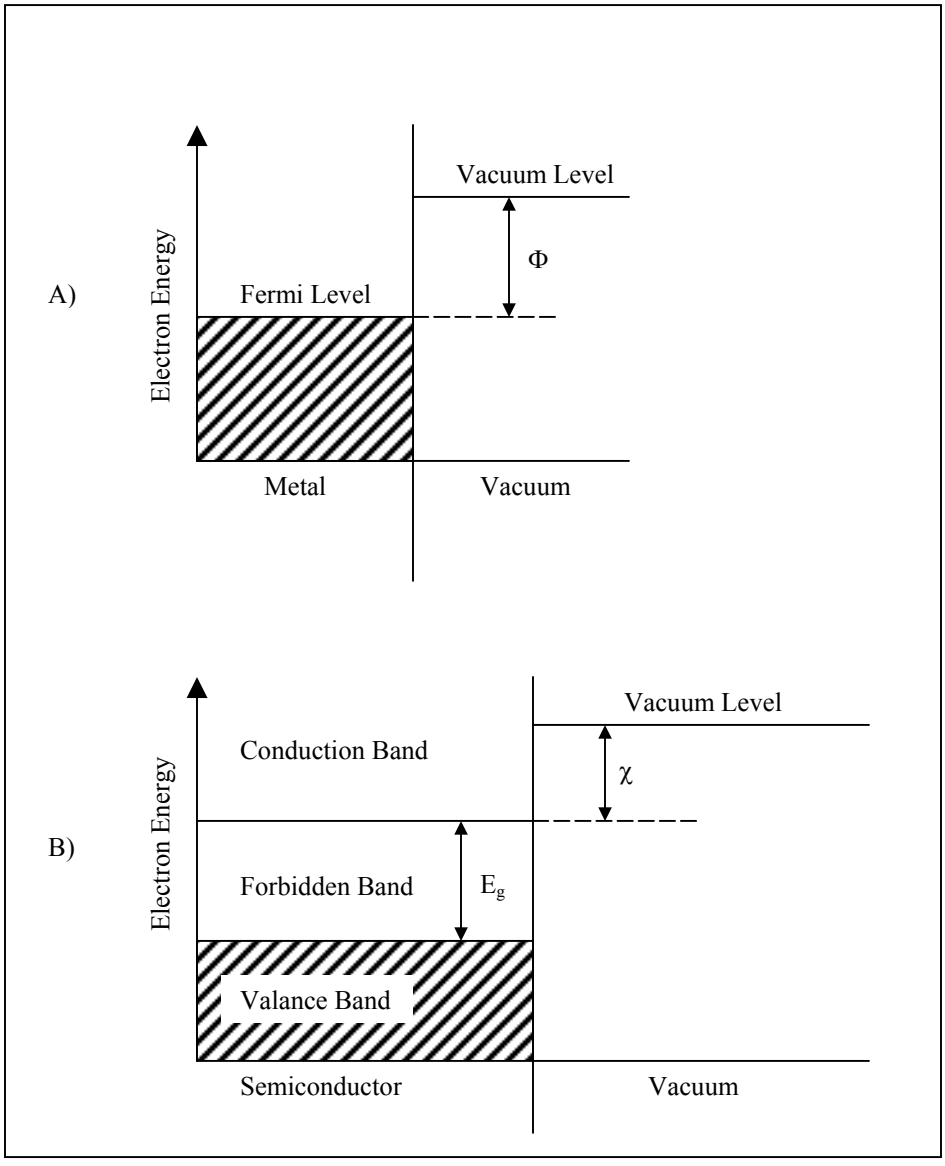

Figure 5.3. The electronic energy structure for a metal is shown on the top diagram and for a semiconductor on the bottom. The minimum energy required to remove an electron from the metal is the difference between the Fermi and vacuum levels and is referred to as the work function ϕ. The minimum energy required to remove an electron from the semiconductor is the sum of the band gap energy E_g and the energy separating the bottom of the conduction band from the vacuum level, referred to as the electron affinity χ.

place for semiconductors, for which the allowed electronic energy levels are in the form of bands [3]. The bands that are totally filled at the temperature of absolute zero are referred to as valance bands and those bands that are empty or only partially filled are referred to as conduction bands. The energy band gap E_g is defined as the energy difference between the top of the valance bands and the bottom of the conduction bands. For a semiconductor, the Fermi energy is defined as the energy at which the probability of occupancy given by the Femi-Dirac distribution equals ½. The Fermi level usually lies somewhere within the forbidden band, but that has no physical meaning. The electron affinity χ, is defined as the energy separating the bottom of the conduction band from the vacuum level. Thus the smallest photon energy that can result in the ejection of an electron from the semiconductor surface is given by

$$h\nu = E_g + \chi \qquad (5.3).$$

The S-series of semiconductor photocathodes extends out in wavelength to about 900 nm.

It is possible to extend photocathode response out to the order of about 1500 nm [5]. By proper surface preparation and doping, the energy bands can be made to bend in the vicinity of the surface such that the vacuum level is made to lie below the conduction band. An electron excited to the conduction band, which makes its way to the surface, will have an energy greater than the vacuum level and will thus be spontaneously ejected from the surface without having to overcome any surface potential. Thus, the smallest photon energy required to eject an electron for these negative electron affinity (NEA) materials would be equal to the band gap energy E_g leading to long wavelength response.

5.1.4 Saturation Effects

The nonlinear response of an ICCD to incident photon flux is referred to as saturation, for which two distinct causes exist. The most prevalent photocathode materials are of the semiconductor type described in Section 5.1.3, above. The photoelectron is not released from the bulk material, but from the surface of the photocathode. When an electron is emitted from the surface, it must be replaced by an electron from the bulk material. This process is necessarily rate limited by carrier lifetime. When the photon flux reaches a sufficiently high level, this rate-limited process of flow of electrons cannot keep up with the rate of incident photons, thus the probability that a given photon will be absorbed and lead to the ejection of a photoelectron is decreased. This has the affect of saturating the response to some degree resulting in nonlinear behavior. This mechanism should not be considered gain saturation, but it is actually a decrease in the quantum efficiency. The reduced quantum efficiency would lead to a decrease from the expected value of the signal-to-noise and therefore, it must be properly accounted for in the noise model.

The second saturation effect is due to the space charge build up at the MCP anode. Saturation by the space charge effect is a phenomenon of gain saturation inside the microchannels caused by the electrostatic repulsion between electrons produced by the multiplication process and newly emitted secondary electrons. This electrostatic repulsion weakens the electric field intensity within the microchannel, thereby suppressing the succeeding electron multiplications. The higher gain voltages have much higher gain gradients and are therefore much more affected relative to low gain voltages. The strip current flowing through the channel walls neutralizes this space charge. The high

resistance of the channel walls, however, limits the current. Thus, it takes a finite time for the charge to be neutralized, which is referred to as dead time. This gain saturation effect occurs when the output current due to electron amplification reaches about 5% of the strip current according to a Hamamatsu specification sheet for MCP's. The lower the MCP resistance the higher the strip current. Normal MCP resistance is on the order of 200 MΩ, but some devices are made with a resistance as low as 30 MΩ. The lower the resistance, however, the more self heating that results, which could be problematic if active cooling was not used. The flux at which saturation occurs decreases with increasing frequency because of the finite dead time. Thus, systems such as the Time-Domain Optical Breast Imager of this dissertation, that use frequencies in the range of 80 MHz would be expected to have relatively low saturation thresholds. This second saturation effect does not directly impact signal-to-noise, as did the first. This is a consequence of the fact that the signal, background and noise that originate prior to the MCP all experience the same gain. It is important to keep in mind that there is a narrow window of operation of the ICCD, particularly for high repetition-rate sources, for which saturation effects will not be appreciable. High flux levels will lead to photocathode saturation effects and high gains can lead to gain saturation effects. This is not necessarily a problem as long as proper account is taken to apply a saturation correction factor to the data. For example, the shape of a given temporal point spread function (TPSF) for a time-domain measurement may be distorted due to saturation effects. The magnitude of the higher amplitude portions of the signal can be attenuated. In addition, the relative peak amplitudes between different source-detector pairs may be out of proportion due to saturation. The system must be calibrated for the exact conditions of

the measurement including the source repetition frequency, MCP gain, source dwell and CCD integration time over the full dynamic range of the CCD. Failure to do this will lead to distortions of the ensemble of TPSF's and will result in poor fits to the forward model.

5.1.5 Photon Noise

Photon noise is fundamental in the sense that it arises not from any imperfection in the detector or any associated electronics, but rather from the detection process itself. The photon noise process can be understood from two conceptually distinct but complimentary points of view. The noise can be viewed as resulting either from the randomness in the arrival rate of the individual photons or from the randomness in the emission time of photoelectrons [3]. This discussion is limited to stable laser sources (which allows the Bose-Einstein nature of a thermal radiation field to be disregarded), so the later perspective is taken. In general, an ideal detector is not realistic, so the quantum efficiency η of the detector is less than unity. Stochastic processes determine whether a particular incident photon produces a photoelectron for quantum efficiencies less than unity. Photon noise, in the limit considered here, is sometimes referred to as shot noise.

In the following discussion, the signal and noise is described in terms of the number of counts to be consistent with the form of the digitized output of the ICCD system. Many authors use current when describing various detectors, particularly with regard to PMT's that produce a current at the anode that can be measured by the voltage drop across a load resistor. For the case of an ICCD, the electrons are converted back to light by the phosphor and subsequently detected by the CCD for which the output is ultimately

digitized, so considering both signal and noise in terms of a digitized number, or in terms of counts, seems reasonable.

For the present discussion, the detector is assumed ideal in the sense that it produces no output in the absence of incident power and no noise except that associated with the randomness of the emission times of the photoelectrons. The emission events are assumed probabilistic in the sense that they are uncorrelated and occur at an average rate

$$\bar{r} = \frac{\eta_{pc}\varepsilon_{(P_s)}\Omega\Gamma P_s}{h\nu} \tag{5.4}$$

where η_{pc} is the photocathode quantum efficiency, $\varepsilon_{(P_s)}$ is the saturation coefficient for the quantum efficiency described in Section 5.1.4, Ω is the open-air ratio, which is the ratio of the total effective microchannel plate active area divided by the total area of the microchannel plate apertures and is typically on the order of 60 to 80%, P_s is the average power incident on the photocathode, h is Plank's constant, ν is the nearly monochromatic frequency of the incident power, and Γ is the effective duty cycle of the intensifier, defined as the ratio of the integrated gate temporal width divided by the laser source pulse-to-pulse period. For a time resolved system, P_s will be a function of the tissue background properties and thickness, gate width, gate delay relative to the zero time reference of the tissue TPSF, the system impulse response, incident laser power per pulse and repetition rate, and system transmission efficiency. The average number of photoevents occurring within an integration time τ (dictated by the CCD or equivalently, source dwell time) is

$$\bar{n} = \bar{r}\tau, \tag{5.5}$$

Thus, the average signal number is given by

$$\overline{n} = \frac{\eta_{pc}\varepsilon_{(P_s)}\Omega\Gamma P_s \tau}{h\nu} \tag{5.6}$$

The actual number occurring within the integration time will fluctuate about this mean. The probability of exactly *n* photoevents occurring within the time τ is given by the Poisson probability distribution [3,4]. It is a property of the Poisson distribution that the variance in the number from the mean value is equal to the mean

$$\overline{(\Delta n)^2} = \overline{n} \tag{5.7}$$

and the rms fluctuation is given as

$$\Delta n_{rms} = (\overline{n})^{1/2} \tag{5.8}$$

The concept of signal-to-noise ratio (SNR) is now introduced. It is a useful construct with which to evaluate the noise character of a given measurement system or subsystem. The signal, in the case of photon noise limited performance, is given by Equation 5.6 and from Equation 5.8, the noise is of the form

$$\Delta n_{rms} = \left(\frac{\eta_{pc}\varepsilon_{(P_s)}\Omega\Gamma P_s \tau}{h\nu} \right)^{1/2} \tag{5.9}$$

The SNR for photon noise limited performance is thus given by

$$SNR = \frac{S}{N} = \frac{\overline{n}}{\Delta n_{rms}} = \left(\frac{\eta_{pc}\varepsilon_{(P_s)}\Omega\Gamma P_s \tau}{h\nu} \right)^{1/2} \tag{5.10}$$

The discussion above has implicitly assumed that all power incident on the photocathode is from the laser source. In practice, this may not always be the case, as there may be background power from other light sources present as well. For example, in the case of optical breast imaging, there will be some finite background signal due to the ambient light conditions. Light that is scattered within the ICCD input objective should

also be considered as a background and should be kept to a minimum by design. The number of photoelectrons that result from the background will have a nonzero variance and will degrade the system-level SNR. In this case, the noise term is modified to account for this variance as

$$\Delta n_{rms} = \left[\frac{\eta_{pc} \varepsilon_{(P_s)} \Omega \Gamma (P_s + P_B) \tau}{h \nu} \right]^{1/2} \tag{5.11}$$

where P_B is the average background photon power incident on the photocathode within its spectral response, or the spectral band of the input bandpass filter if there is one. The SNR can be improved by decreasing the duty cycle for the same integrated number of source photons, by increasing source intensity per pulse (limited by the restrictions of the minimum permissible skin exposure and perhaps by saturation effects). This is a consequence of the fact that only the background signal collected during the photocathode open-gate time adds to the average detected background, with the exception of source photons scattered by the camera objective. This is the basis of pulsed-gated detection, which is a signal collection technique widely used to improve system-level SNR in the Photonics field. It would be prudent to incorporate a spectral bandpass or long-pass filter in front of the photocathode to exclude background from sources outside the spectral region of interest. In the case of the Time-Domain Optical Breast Imaging System, the bandpass would be limited to between 750 and 850 nm. Typical intensifier photocathode quantum efficiency falls off sharply for these near infrared wavelengths, so the advantage of a filter is even greater. The effect of the background on the limited dynamic range of the ICCD should also be considered. Additionally, one could place low cost near infrared absorption plastic sheets over any ambient lights to further mitigate background effects. It has been assumed here, that the background is substantially

constant over the full measurement period. If the background is modulated on a time scale small relative to the total measurement period, such as might be the case for overhead AC fluorescent or incandescent lights, one must take special precautions, as such background modulations may be difficult to correct for. Now the background-modified SNR is

$$SNR = \left(\frac{\eta_{pc} \varepsilon_{(P_s)} \Omega \Gamma \tau}{h\nu} \right)^{1/2} \frac{P_s}{\left(P_s + P_B\right)^{1/2}} \qquad (5.12).$$

In the event that the background power is on the order of or larger than the signal, the system is referred to as background limited.

5.1.6 Intensifier Dark Noise

Dark noise in the intensifier is a consequence of the fluctuation in the number of counts in the absence of any light incident on the photocathode. The two dominant noise sources in the ICCD's intensifier are shot noise in the dark count and noise introduced due to the process of electron amplification. At room temperature, the dark count is primarily due to thermionic emission, but emission due to cosmic ray events, natural radioactivity of the glass substrates, and ionization of residual gas within the intensifier can dominate the dark noise if the temperature of the photocathode is reduced to a level where thermionic emission is sufficiently suppressed.

The Richardson-Dushman equation provides a reasonable estimate of the average rate at which electrons are thermally ejected from the surface of a metallic photocathode as

$$\bar{r} = 4\pi m \left(kT\right)^2 h^{-3} A e^{-\Phi/kT} \qquad (5.13)$$

where m is the rest mass of an electron, k is Boltzman's constant, T is the absolute temperature, h is Plank's constant, A is the photocathode area measured in square centimeters, defined by the diameter of one microchannel, and Φ is the work function of the metal photocathode[3]. As mentioned earlier, the photocathodes for intensifiers are typically made of classical semiconductor materials. The actual thermionic emission level is also dependent on surface application techniques, so there is no exact formula. Nonetheless, Equation 5.13 should give a reasonable upper bound and order-of-magnitude estimate of thermionic emission for semiconductor photocathodes.

The noise contribution due to the thermionic emission can be considered to result from an equivalent power incident on the photocathode of $P_{D(int)}$. The average rate can be expressed as

$$\bar{r} = \frac{\eta_{pc}\varepsilon_{(P_s)}\Omega P_{D(\mathrm{int})}}{h\nu} \qquad (5.14).$$

This equivalent dark power can be expressed by equating 5.13 and 5.14 above as

$$P_{D(\mathrm{int})} = \left(\frac{4\pi m\nu}{\eta_{pc}\varepsilon_{(P_s)}\Omega h^2}\right) A(kT)^2 e^{-\Phi/kT} \qquad (5.15).$$

Now the total effective power that contributes to the noise is given by

$$P_{noise} = P_s + P_B + P_{D(\mathrm{int})} \quad . \qquad (5.16)$$

Figure 5.4 shows the equivalent thermionic power incident on the photocathode as well as the equivalent photon flux. The SNR can now be written in a form accounting for both background power and equivalent thermionic emission power as

$$SNR = \left(\frac{\eta_{pc}\varepsilon_{(P_s)}\Omega\Gamma\tau}{h\nu}\right)^{1/2} \frac{P_s}{\left(P_s + P_B + P_{D(\mathrm{int})}\right)^{1/2}} \qquad (5.17).$$

It is assumed here that the thermionic emission is the primary dark noise source, but Equation 5.16 could easily be extended to include other sources described above, such as cosmic ray events. In a typical intensifier, which is not actively cooled, higher MCP gain voltages lead to increased heating of the electrodes, which can exacerbate the thermionic emission contribution to the noise.

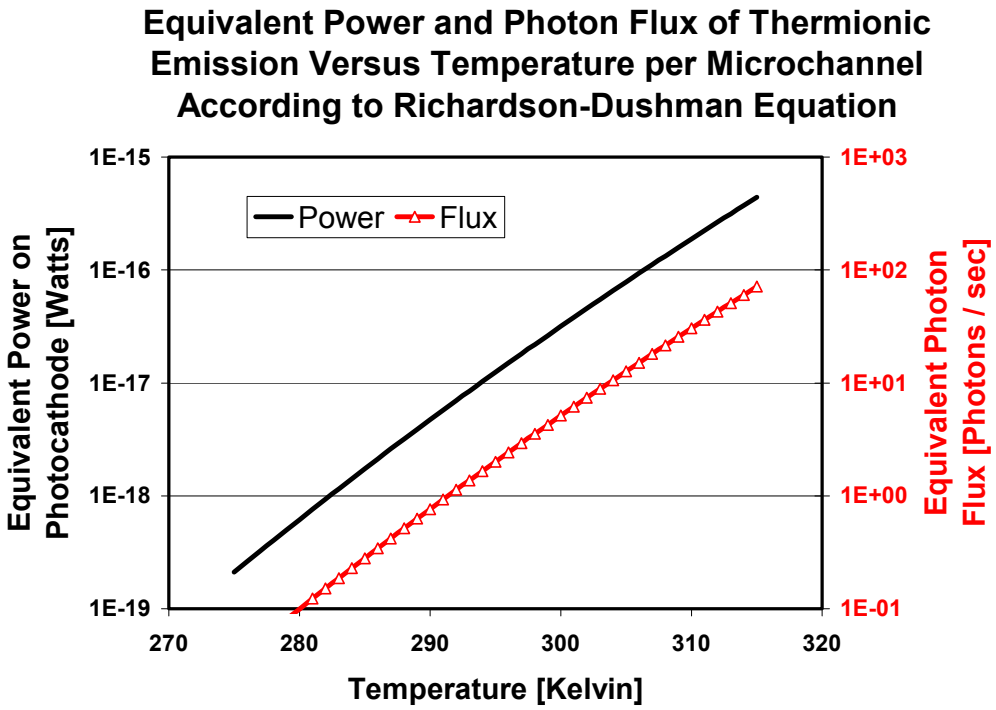

Figure 5.4. The equivalent power and photon flux is shown for the case of a quantum efficiency η of 0.04. The response is based on the Richardson-Dushman equation for a metal of work function Φ and establishes a reasonable upper limit and order of magnitude estimate for the classical semiconductor photocathodes such as the S20.

The contribution from the electron gain process itself on the total dark noise is now considered. Ideally, the gain process would be noiseless, however, there is a finite reduction in SNR because the actual number of secondary electrons created in the primary electron impact is a stochastic quantity. The electron amplification process can be shown to decrease the SNR by the quantity [3], as shown in Figure 5.5, as

$$\gamma = \left(\frac{\delta_1}{\delta_1 - 1} \right)^{1/2} \tag{5.18}$$

under the assumption that the variance of the number of secondary electrons at any point along the channel is equal to the mean number of secondary electrons δ (as would be the case for a Poisson distribution) and under the assumption that N_{eff}>>1 [4]. The fluctuation is dominated by the variance in the first secondary emission event as it has the fewest total number of secondary emitted electrons as indicated by the subscript on δ.

The complete expression for the SNR of the photocathode and microchannel plate can now be written as

$$SNR = \left(\frac{\eta_{pc} \varepsilon_{(P_s)} \Omega \Gamma \tau}{h\nu} \right)^{1/2} \frac{1}{\gamma} \frac{P_s}{\left(P_s + P_B + P_{D(\text{int})} \right)^{1/2}} \tag{5.19}.$$

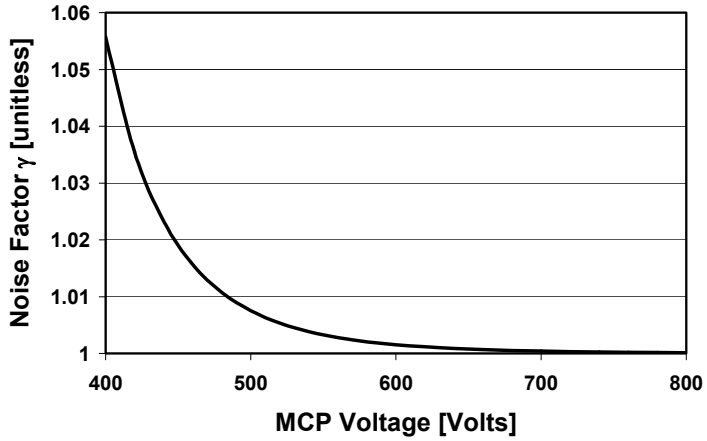

Figure 5.5. The noise factor γ is shown as a function of MCP voltage for a secondary emission ratio of 1.3 at 400 Volts. Typical values of gain would be on the order of 500 to 700 Volts, so this noise factor will generally have little effect on the SNR.

It is interesting to note that since δ increases with voltage, the noise factor γ results in higher SNR's for higher gains. High gains, however, would also amplify noise sources such as thermionic emission, which could be problematic due to the limited dynamic range of the ICCD output.

5.1.7 CCD noise

The SNR of Equation 5.19 takes the model up to the phosphor, which is the last element of the intensifier. The electron cloud that exits the microchannel plate is accelerated by a large potential toward the phosphor. Each electron that strikes the phosphor generates approximately 200 green electrons (P43 phosphor). A 2:1 magnification relay lens is used to collect a fraction ε_{relay} of these photons and image them onto the active area of the CCD sensor. In some systems, a coherent fiber-optic taper is used in place of the relay lens to achieve a higher effective numerical aperture and thereby a higher efficiency.

The CCD is a detector having its own characteristic noise properties, distinct and in addition to those of the intensifier. The CCD noise can be categorized as photon (shot) noise, dark noise from thermally generated carriers in the semiconductor material that comprise the photosensitive elements of the CCD, and readout noise that comes about as a consequence of the process of shifting accumulated charge created by the photocurrent out of the device followed by amplification. The digitization noise of the A/D converter can be included in the readout noise as an uncertainty of 1 count in 4096 for a 12-bit camera. The dark noise and to a lesser extent, the readout noise, is a function of the CCD operating temperature. The counts due to accumulated dark current increase with integration time. Typically, ICCD cameras are thermoelectrically cooled to reduce CCD dark noise to near negligible levels. The readout counts, and the associated variance, are not affected by integration time.

The signal on the CCD due to the intensifier is now considered, as given by

$$\overline{n}_s = \frac{\eta_{pc}\varepsilon_{(P_s)}\Omega\Gamma P_s\tau}{h\nu} G_{MCP(P_s,V)} G_{Phos}\varepsilon_{relay}\eta_{CCD} \qquad (5.20)$$

where G_{Phos} is the electron-to-photon gain for the phosphor and η_{CCD} is the quantum efficiency of the CCD. A dependency of the MCP gain on both the incident photon flux and the MCP gain voltage was added, denoted by the subscripts P_s and V, to account for the gain saturation effects described in Section 5.1.4, above.

In a way analogous to the discussion of dark signal for the intensifier, the CCD dark signal power can be defined as $P_{D(CCD)}$. The root mean square (rms) noise count prior to the microchannel plate is given by substitution of Equation 5.16 into Equation 5.11 as

$$\Delta n_{rms} = \left(\frac{\eta_{pc} \varepsilon_{(P_s)} \Omega \Gamma \left(P_s + P_B + P_{D(\mathrm{int})} \right) \tau}{h \nu} \right)^{1/2} \qquad (5.21).$$

This noise would experience the same gain as the signal of Equation 5.20, giving a value for the noise count from the intensifier on the CCD of

$$\Delta n_{rms(\mathrm{int})} = \left(\frac{\eta_{pc} \varepsilon_{(P_s)} \Omega \Gamma \left(P_s + P_B + P_{D(\mathrm{int})} \right) \tau}{h \nu} \right)^{1/2} G_{MCP(P_s,V)} G_{Phos} \varepsilon_{relay} \eta_{CCD} \gamma \qquad (5.22).$$

In addition to the noise from the intensifier, the shot noise in the green photon intensity from the phosphor incident on the CCD must be considered as

$$\Delta n_{rms(CCD)} = \left(\frac{\eta_{pc} \varepsilon_{(P_s)} \Omega \Gamma \left(P_s + P_B + P_{D(\mathrm{int})} \right) \tau}{h \nu} \right)^{1/2} \left(G_{MCP(P_s,V)} G_{Phos} \varepsilon_{relay} \eta_{CCD} \gamma \right)^{1/2}$$

(5.23)

The noise factor γ has been added. The total noise of the ICCD system would be given by the root sum square (rss) of the individual uncorrelated noise sources as follows

$$\Delta n_{rms(ICCD)} = \left(\left(\Delta n_{rms(\mathrm{int})} \right)^2 + \left(\Delta n_{rms(CCD)} \right)^2 + \left(\frac{\eta_{CCD} P_{D(CCD)} \tau}{h \nu_{phos}} \right) + \left(\Delta n_{rms(readout)} \right)^2 \right)^{1/2}$$

(5.24)

where the third term represents the shot noise due to the CCD dark signal, for which the frequency of the intensifier spectrum ν_{phos} has been designated. The noise fluctuation due to the CCD readout is designated as $\Delta n_{rms(readout)}$. This gives an expression for the ICCD system-level SNR as

$$SNR_{ICCD} = \frac{\frac{\eta_{pc}\varepsilon_{(P_s)}\Omega\Gamma P_s\tau}{h\nu} G_{MCP(P_s,V)} G_{Phos}\varepsilon_{relay}\eta_{CCD}}{\left[\left(\eta_{pc}\varepsilon_{(P_s)}\Omega\Gamma\frac{\left(P_s+P_B+P_{D(\mathrm{int})}\right)\tau}{h\nu}\right)\left[\left(G_{MCP(P_s,V)}G_{Phos}\varepsilon_{relay}\eta_{CCD}\gamma\right)^2+\left(G_{MCP(P_s,V)}G_{Phos}\varepsilon_{relay}\eta_{CCD}\gamma\right)\right]+\left(\frac{\eta_{CCD}P_{D(CCD)}\tau}{h\nu_{phos}}\right)+\left(\Delta n_{rms(readout)}\right)^2\right]^{1/2}}$$

(5.25).

It is assumed here that there is negligible background power incident on the CCD, as it is enclosed and that the unwanted scattering from the phosphor is sufficiently suppressed by good relay lens design as to be negligible. Typically, the MCP gain of the intensifier would be sufficiently high that the shot noise from the green photon signal on the CCD could be neglected in comparison with the shot noise from the CCD. The shot noise from the green photons on the CCD is included here for generality.

5.1.8 Affect of ICCD Point Spread Function on Signal-to-Noise Ratio

In the discussion above, no allowance was made for the effect of the ICCD's spatial point spread function (SPSF) on the SNR. A point image, or delta function spatial input, on the photocathode would not produce a point image on the CCD, but would be smeared out over many pixels due to depressive effects at each step along the path between the two points, resulting in a degradation in SNR. The gap between the photocathode and MCP input, the gap between the MCP output and the phosphor, the finite phosphor layer

thickness, and the optical relay lens diffraction and geometrical blur all contribute by varying degrees to the smearing out of the ICCD's SPSF.

If a circular input aperture function to the ICCD is considered, and a Gaussian function is used to represent the ICCD system SPSF, then the SNR degradation factor has been shown to be

$$F_{SPSF} = \frac{\left[1 - \exp\left(\frac{-\pi d^2}{2b^2}\right)\right]}{\sqrt{\left[1 - \exp\left(\frac{-\pi d^2}{b^2}\right)\right]}} \tag{5.26}$$

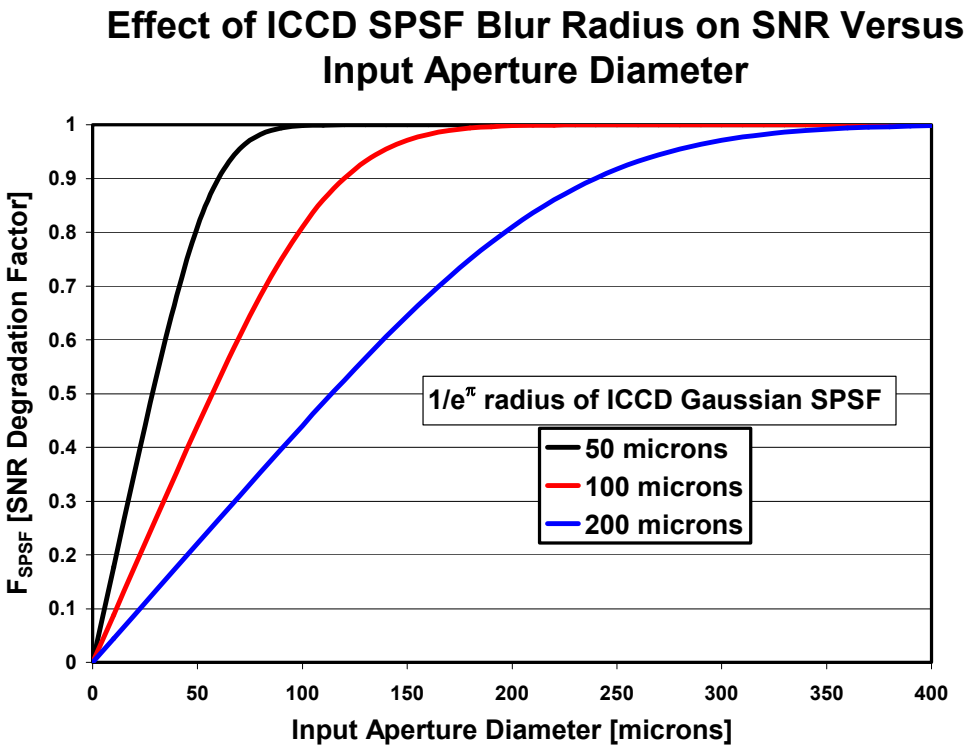

Figure 5.6. The affect of the blur radius of the Gaussian SPSF on the Signal-to-Noise is shown as a function of the input aperture diameter.

where *d* is the diameter of the input aperture, such as the image of an optical fiber, and b is the $1/e^{\pi}$ radius of the ICCD's Gaussian SPSF [1]. An example of the effect on the SNR for blur radii of 50, 100 and 200 microns is shown in Figure 5.6. A typical blur radius of a 2nd Generation Proximity Focused ICCD would be on the order of 100 microns, which for an input fiber of 60 microns, would result in almost a 50% reduction in the SNR. For the case of a 400 micron fiber, as was used in the breast imaging system described in Chapter 4, the degradation is negligible.

This factor could be extended to include the SPSF of the objective lens system on the front end of the ICCD as well.

5.1.9 Affect of Pixel Binning on Signal-to-Noise Ratio

The SNR could be improved by binning the signal from a number of CCD pixels. For example, in the case of the Time-Domain Optical Breast Imaging System, an 8 by 8 pixel binning was used. If it was assumed that the signal and noise were of the same magnitude on each binned pixel and that the noise was uncorrelated, the SNR would improve by the square root of the number of pixel measurements, assuming shot noise limited performance. In the case of the breast imaging system, a 400-micron input fiber was used, which extended over more than 30 CCD pixels in diameter, or about 4 times the dimensions of the 8 by 8 binning. A further binning of the image file on the order of 4 by 4 was thus necessary. This second binning step was not part of the measurement, but was actually post-detection signal processing on the stored image file. It is included in this section to treat binning as a whole.

The distinction is made between on-chip binning and post-readout binning, as they have different effects on the SNR. On-chip binning refers to binning that takes place within the camera, as opposed to within the computer.

The normal procedure for reading out the electric charge pattern stored in the CCD is pixel by pixel. In this procedure, a single parallel transfer places the accumulated charges from one row of pixels into the serial output register. The output register is then emptied by transferring the charge from each element of the output register to the output amplifier and then reading the amount of charge in each amplifier. If one parallel transfer is immediately followed by others, without reading out the output register first, then the charges in the second or subsequent row are added to the charges already in the output register. This constitutes the process of binning. It is possible to add charges in the serial output register in exactly the same way.

Binning the parallel transfer electrodes is known as parallel binning and binning the serial transfer electrodes is known as serial binning. Sometimes parallel and serial binning is referred to as vertical and horizontal binning, reflecting the way that CCDs are oriented to produce a TV picture.

In many CCDs, the charge capacity of the CCD output register is significantly larger than that of the individual imaging pixels. This allows binning into the output register to reach higher peak signals without saturation.

Any parallel binning factor may be combined with any serial binning factor. For example, in the breast imaging system an 8x8 charge binning was used. This means that a sequence of eight parallel transfers was followed by a serial readout where eight pairs of eight pixels at a time were transferred to the CCD output node to be measured together.

The binning of the charge pattern is essentially a noiseless process and leads to higher signal levels in the output register and significantly reduces the readout time, which may be important in some applications.

Noise currents in the CCD output amplifier generate the readout noise level, which provides the lower limit of sensitivity for a scientific grade CCD camera system. The advanced signal processing used in these CCD imaging systems ensures that this readout noise is essentially a constant noise added to the signal from each readout element and is essentially independent of temperature. The fixed readout noise is added once for each output amplifier read operation and is unaffected by where the charge it is measuring came from.

The CCD may be operated as to allow for *n* rows to be added into the serial output register and for *m* serial output register elements, corresponding to the CCD columns, to be added into the output amplifier. This is described as binning *n* x *m* pixels on-chip, and the readout of this signal, which will be *n* x *m* times the signal in a single pixel for uniform illumination, will only have one unit of readout noise added by the output amplifier.

There are a number of advantages to binning the CCD image on-chip by *n* x *m*. The read noise is associated with each pixel read. Binning by *n* x *m* on a full resolution image by pixel averaging in the computer, gives an image with the same resolution as an on-chip binned image. The readout noise, however, will be higher in comparison with on-chip binning. If the readout noise per pixel is *s* electrons RMS, it will be *s* for the on-chip binned image but $s\sqrt{mn}$ for the post-readout binned image. Therefore, on-chip binning optimizes the readout noise. Another advantage is that the signals that are read out will

be larger by a factor of up to *n* x *m* for a uniformly illuminated image. Another advantage is that the readout time for a full image will be much shorter, almost in proportion to the number of elements read out. The prime disadvantage of on-chip binning is that it is not possible to recover the original spatial resolution, so one must trade off SNR versus spatial resolution for a particular application. In the case of the Time-Domain Optical Breast Imaging System, it was desirable to maximize the SNR. In fact, if the camera were capable of performing larger binning operations on-chip, the SNR would have been improved. As an example of the advantage of on-chip binning, if a signal count of 100 per pixel and a readout fluctuation of 5 counts was considered, for 8 by 8 on-chip binning, the SNR would have been 79.8 compared to 71.6 for post-read binning.

The assumption that the noise from pixel to pixel is uncorrelated is not completely valid. This is a consequence of the fact that the MCP resolution elements are larger than those of the CCD and that the ICCD has a finite SPSF that smears the signal and noise across some effective number of CCD pixels. Thus nearest neighbors will have noise components that are correlated to some degree.

Now that the effects on the SNR of on-chip versus post-readout binning are appreciated, it is necessary to treat the effects separately. The improvement factor F_{bin} for the shot noise limited binning effect on SNR will now be

$$F_{bin} = \sqrt{(n_{CCD} - n'_{CCD})(m_{CCD} - m'_{CCD})}\sqrt{(n_{image} - n'_{image})(m_{image} - m'_{image})} \qquad (5.27).$$

where n_{CCD} is the number of on-chip binned rows in the CCD, m_{CCD} is the number of on-chip binned columns in the CCD, n'_{CCD} is the effective number of noise-correlated rows on the CCD for which $n'_{CCD} \leq (n_{CCD} - 1)$, m'_{CCD} is the effective number of noise-correlated columns on the CCD for which $m'_{CCD} \leq (m_{CCD} - 1)$, n_{image} is the number of

binned rows on the image file, m_{image} is the number of binned columns on the image file, n'_{image} is the effective number of noise-correlated rows on the image file for which $n'_{image} \leq (n_{image} - 1)$, and m'_{image} is the effective number of noise-correlated columns for the image file for which $m'_{image} \leq (m_{image} - 1)$. Thus, if the noise is totally correlated over the on-chip bin range, the first term in F_{bin} becomes unity and does not improve the SNR. Both n'_{image} and m'_{image} would be expected to be non-zero in the case that no on-chip binning was performed. In the case where on-chip binning was greater in extent than the number of noise-correlated pixels, both n'_{image} and m'_{image} would be expected to be zero.

The effect of the reduced readout noise described above for on-chip binning must also be accounted for. This would improve the SNR further, but this term cannot be incorporated into Equation 5.27, as its effect must be related to the signal level. Equation 5.25 must be modified to include the multiplicative effect of the binning. This is done by dividing the readout noise by n_{CCD} and m_{CCD}. Thus, the relative contribution of the readout noise would decrease with increased binning.

5.1.10 Affect of MCP Gain Voltage Fluctuations on the Signal-To-Noise Ratio.

The gain of the microchannel plate is a very strong function of the voltage between the device electrodes as was noted in Equation 5.1. Fluctuations in the gain voltage with a period small relative to the CCD integration time would be manifest as fluctuations in the signal and would be indistinguishable from shot noise. For MCP voltage fluctuations on the order of 5% or less, the SNR due solely to the gain fluctuations is given by

$$SNR_{MCP(V)} = \frac{\sqrt{\tau / T_L}}{N_{eff}\sigma_{MCP(V)}} \qquad (5.28)$$

where $\sigma_{MCP(V)}$ is the standard deviation of the MCP gain voltage in percent. The value of N_{eff} is typically on the order of 6 to 10, so it is critical to the proper function of the ICCD to maintain a very stable and low-noise gain voltage to the MCP. This effect will be added to the SNR_{ICCD} in a root-sum-squared sense as will be shown below.

5.1.11 Effect of Source Fluctuations

Generally, any fluctuations that are short in time scale relative to the integration time of the ICCD, would not be resolved by the system and would therefore constitute noise and degrade the SNR. Fluctuations that are slow relative to the integration time would be considered source drift and could be divided out by appropriate sampling of the source intensity entering the source fiber. Any noise on the source monitor would necessarily degrade the system-level SNR. There are two potential sources of fluctuations in the laser source intensity for the case of the breast imaging system. The first is pulse-to-pulse fluctuations in the laser output. A mode-locked Ti:Sapphire laser operating at a pulse repetition frequency of 80 MHz would result in 8 million pulses for a typical 100 msec integration time. For 8 million pulses, a pulse-to-pulse standard deviation for the laser amplitude equal to 10% of the mean would be reduced to an insignificant 0.0035%, as the standard deviation would decrease as the square root of the number of pulses. Thus in the case of time-domain system, this noise term can be neglected, but it is included here for generality, in the event that a much lower repetition rate source might be used. The second cause of source fluctuations is potentially due to the oscillatory nature of the galvanometer's closed-loop servo control. Even when the galvanometer mirrors are positioned to a fixed angle, they dither slightly in angle, to allow the closed-loop position

feedback system to function. If the image of the laser on the input fiber is on the order of the fiber diameter, or if the edge of the image overlaps the fiber diameter, the light coupled into the fiber could be modulated. Typically these oscillations would be in the 10's of kHz, so many oscillations would occur within a 100 msec integration time. If the standard deviation due to fluctuations of the galvanometer were on the order of 10% of the mean intensity, the standard deviation for an integration time of 100 msec would be reduced to the order of 0.3%. This value may be of significance and should be included in the analysis. Expressions can be written for the SNR due to laser source fluctuations $SNR_{S(L)}$ and galvanometer source fluctuations $SNR_{S(G)}$ as

$$SNR_{S(L)} = \frac{\sqrt{\tau / T_L}}{\sigma_L} \tag{5.29}$$

and

$$SNR_{S(G)} = \frac{\sqrt{\tau / T_G}}{\sigma_G} \tag{5.30}$$

where σ_L and σ_G are the standard deviation of the laser source intensity due to pulse-to-pulse laser output and galvanometer dithering, respectively and are expressed in percent, and T_L and T_G are the periods of fluctuation for the laser pulses and galvanometer oscillations, respectively. These SNR terms will also be added below, to the SNR_{ICCD} in a root-sum-squared sense.

5.1.12 System-Level Signal-To-Noise Ratio

The SNR factors of Equations 5.26, 5.27, and the effect of on-chip binning described in Section 5.1.9 can be incorporated into Equation 5.25, for the total ICCD SNR as

$$SNR_{ICCD} = \frac{\frac{\eta_{pc}\varepsilon_{(P_s)}\Omega\Gamma P_s\tau}{h\nu} G_{MCP(P_s,V)} G_{Phos}\varepsilon_{relay}\eta_{CCD}\left(F_{SPSF}F_{bin}\right)}{\left[\left(\eta_{pc}\varepsilon_{(P_s)}\Omega\Gamma\frac{\left(P_s+P_B+P_{D(\mathrm{int})}\right)\tau}{h\nu}\right)\left[\left(G_{MCP(P_s,V)}G_{Phos}\varepsilon_{relay}\eta_{CCD}\gamma\right)^2+\left(G_{MCP(P_s,V)}G_{Phos}\varepsilon_{relay}\eta_{CCD}\gamma\right)\right]+\left(\frac{\eta_{CCD}P_{D(CCD)}\tau}{h\nu_{phos}}\right)+\left(\frac{\Delta n_{rms(readout)}}{n_{CCD}m_{CCD}}\right)^2\right]^{1/2}}$$

(5.31).

The total system-level SNR would be determined by combining Equations 5.28 through 5.31 in a root-sum-squared sense as

$$SNR_{system} = \frac{1}{\sqrt{SNR_{ICCD}{}^{-2} + SNR_{MCP(V)}{}^{-2} + SNR_{S(L)}{}^{-2} + SNR_{S(G)}{}^{-2}}} \qquad (5.32).$$

5.2 Theoretical SNR Analysis

The equations of Section 5.1 can be used to predict SNR behavior under various conditions to derive insight into the interpretation of measured data that will be presented in Chapter 6. The purpose of developing the noise model in Section 5.1 and of predicting SNR behavior in this section is to understand under what conditions the contrast-to-noise ratio (CNR) of the reconstructed optical properties of tissue or of a tissue phantom can be optimized. The assumption here is that optimizing the SNR of the measurement will lead to optimization of the reconstructed optical properties. Other parameters that come into consideration for optimizing CNR are the trade-offs between the number and positions of source fibers and the number and relative positions of the gate delays. These trade-offs will be discussed further in Chapter 7. This section focuses on instrument SNR.

The noise analysis that was developed in Section 5.1 does not address the uncertainty in the time, only that of amplitude. It was noted in Chapter 3 that the time-domain and frequency domain measurements are related through the Fourier Transform. Frequency domain measurements are comprised of both amplitude and phase information. Any noise

on the phase would result in a degradation of the reconstructed optical properties. The uncertainty in the phase is equivalent to an uncertainty in the time for the time-domain. Thus, any uncertainty in the time between the measurements of individual delays that build up a complete TPSF in the time-domain system would be expected to lead to degradation in the reconstructed optical properties. The uncertainty in the timing of the Time-Domain Breast Imaging System is not included in the noise model. It is limited by system jitter, which is specified by the manufacturer to be less than 25 psec.

Figures 5.7 through 5.10 represent plots of Equation 5.31 with different amounts of noise for obtaining insight into noise behavior that will prove useful for interpretation of real data presented in Chapter 6. The plots will also provide insight into understanding the measurement tradeoffs, such as voltage gain versus integration time. In all cases, $\varepsilon_{(P_s)}$, Ω , F_{SPSF}, and F_{bin} have been set to unity, along with the amount of binning. In each of the four figures, plot (A) represents photon noise only, (B) indicates the effect of adding an equivalent CCD dark power of 1 x 10^{-15} W in addition to the photon flux, (C) represents the effect of adding an equivalent total background or dark power of 3 x 10^{-15} W onto the photocathode in addition to the signal photon flux, and (D) represents the effect of adding 5 counts of readout noise in addition to the photon flux. The signal for each MCP gain voltage, in the cases of Figures 5.7, 5.8, and 5.10, is set to a maximum of 3000 counts to be within the limited dynamic range of our 12 bit camera system. Figure 5.9 sets the count to 3000 for each of the four integration times for 800 volts MCP gain voltage.

Figure 5.7 (A) shows the SNR plotted versus integration time over a range from 10 to 1000 msec for MCP gain voltages ranging from 400 to 800 Volts. The slope of the linear response plotted on a log-log scale indicates a square root dependence of the SNR on integration time, as we would expect for photon noise-limited performance. The narrowing of the distance between lines of increasing MCP gain voltage reflects the functional form of the gain response that is described by Equation 5.1, above. The reason

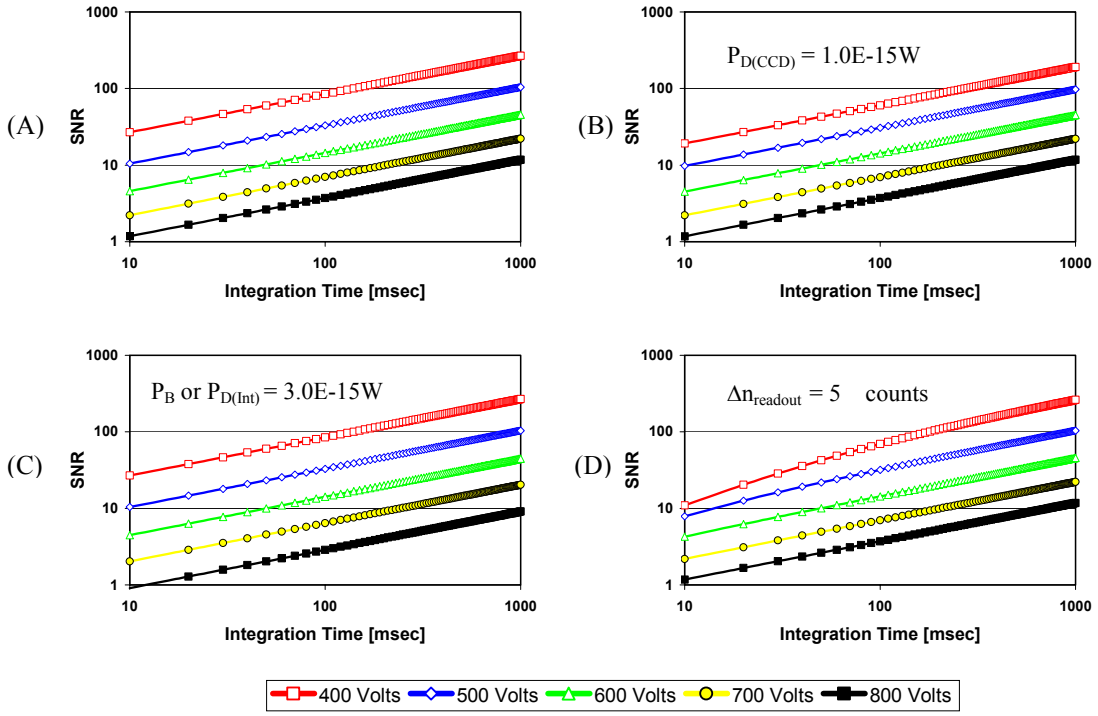

Figure 5.7. A sensitivity analysis is shown for the theoretical predictions of SNR versus integration time for several MCP gain voltages. Plot (A) shows the result of signal photon noise and excess MCP noise only. The other plots add noise in the proportions noted in the plots.

that lower MCP gain voltages have a higher SNR is that for a maximum signal of 3000 counts, the lower voltages and thereby lower gains reflect better photon statistics. The only significant effect of adding dark power from the CCD in plot (B) is the downward shift in the 400 volt MCP gain as a consequence of the square dependence of the gain for

the first noise term in the denominator of Equation 5.31. Plot (C) is shown to decrease SNR primarily for the case of 800 volts MCP gain due to the small number of photons at this high gain in comparison to the magnitude of the background power or dark power from the photocathode. Plot (D) of Figure 5.7 shows the greatest effect for the lower voltages, again due to the square dependency of the first term, but we see the effect is

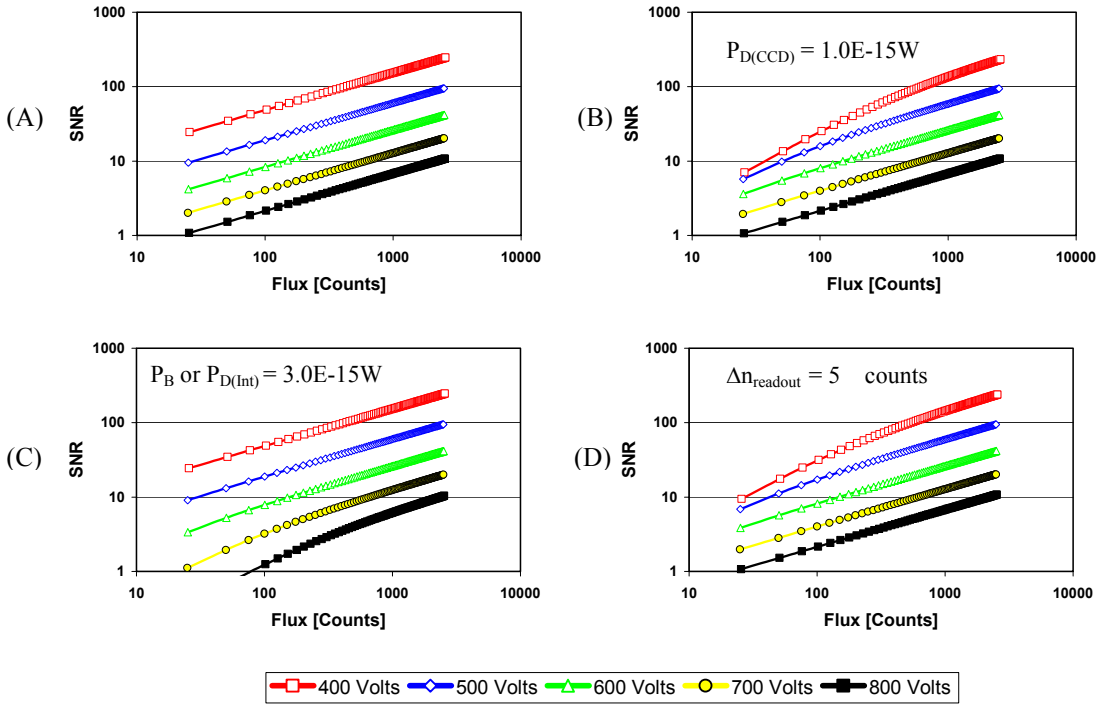

Figure 5.8. A sensitivity analysis is shown for the theoretical predictions of SNR versus signal flux for several MCP gain voltages. Plot (A) shows the result of signal photon noise and excess MCP noise only. The other plots add noise in the proportions noted in the plots.

most significant for lower integration times. This is a consequence of the fact that the readout noise does not scale with the integration time, as did the CCD dark power. Thus, because the lower integration times have proportionally lower counts, they are more affected by readout noise than the higher integration times. Of course, this is not directly a function of the integration time, but reflects the maximum signal being set at the highest integration time. For any given real measurement, this readout noise will set the lower

limit of SNR for low signal counts. In our breast imaging system, we are interested in determining the signal from a range of fiber detector positions, thus detector positions located further from the source would ultimately be limited by readout noise, given

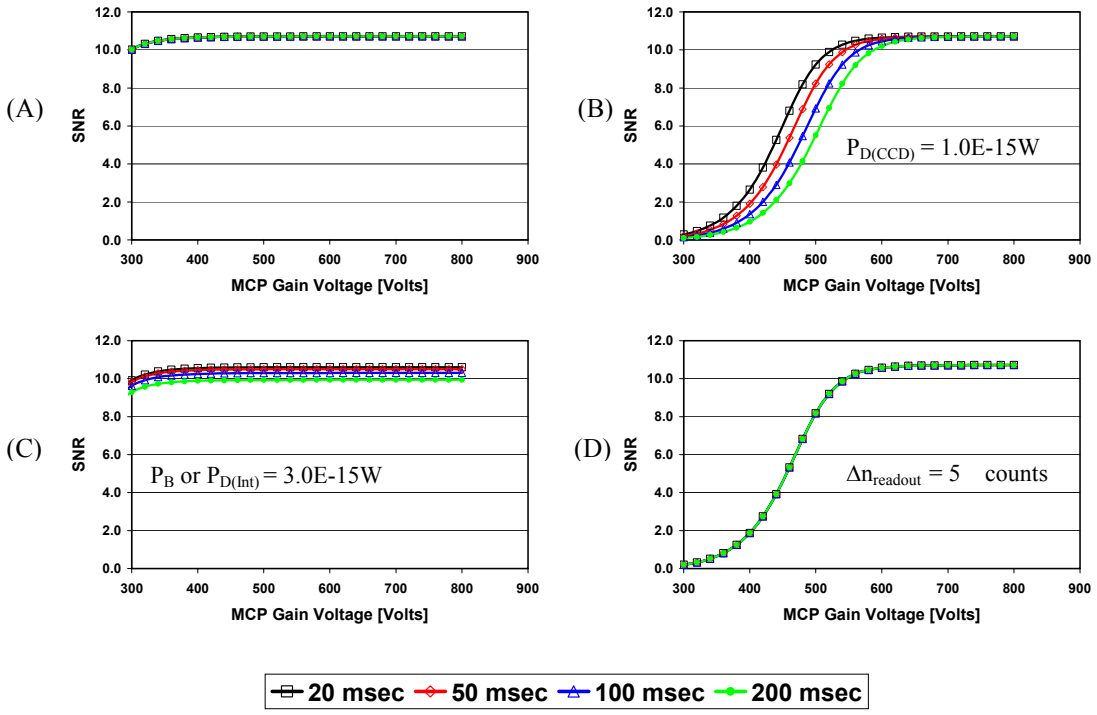

Figure 5.9. A sensitivity analysis is shown for the theoretical predictions of SNR versus MCP gain voltage for several integration times. Plot (A) shows the result of signal photon noise and excess MCP noise only. The other plots add noise in the proportions noted in the plots.

sufficiently high photon statistics.

Figure 5.8 shows plots of SNR versus increasing signal photon flux for a range of MCP gain voltages between 400 and 800 volts, all at an integration time of 100 msec. The slope of the log-log plot of (A) indicates a square root dependence of the SNR on the flux as expected for photon noise-limited performance. Plots (B) and (D) show a similar noise behavior, as both noise terms are independent of the flux. In both cases, the effect of added noise is greatest at low flux and low gains, again due to the square dependence on the gain. Plot (C) shows very little effect of adding either background or dark power

on the photocathode for low MCP gain voltages because the signal power is high relative to these noise powers. At high voltages, however, the signal power is much lower and begins to have competition from these other noise powers. Thus, a fall off is observed in SNR predominantly for the high MCP gain voltages and low flux.

Figure 5.9 shows plots of the SNR versus MCP gain voltage for a range of integration times between 20 and 200 msec. The signal counts were set to 3000 at 800 volts gain for all integration times. In any given plot, the only parameter that is changed is the MCP gain voltage. Plot (A) reflects photon noise and excess noise only. The slight fall off in SNR for low gain voltages is a consequence of the increased excess noise. Plot (B) can be understood by noting that the photon noise begins to be dominated by the CCD dark power for decreasing MCP gain voltages. The longer integration times show a faster fall off with decreasing gain due to the lower number of photons. Plot (C) shows a downward shift for increasing integration times, as the relative proportion of the background or dark signal from the photocathode increases for increasing integration time. Plot (D) looks similar to (C), however, there is no dependency on integration time, as the readout is independent of integration time. This type of plot is very sensitive to CCD dark signal noise and to the CCD readout noise and therefore should prove useful in the fitting of real data described in Chapter 6.

Figure 5.10 shows plots of the SNR versus integration time for constant total integrated signal photons for a range of MCP gain voltages between 400 and 800 volts. Plot (A) indicates that for signal photon noise and excess noise only, the SNR is constant with integration time. For plot (B), dark signal power from the CCD has been added. This leads to a decrease in SNR with increasing integration time predominantly for lower

gains. This is a consequence of the effect of the square dependence on the gain for the first noise term and of the fact that the noise contribution from the CCD dark signal increases with increasing integration time. In the case of plot (C), we see that the presence of background and dark signal power on the photocathode becomes appreciable relative to the signal power at high MCP gain voltages. The integration time dependence

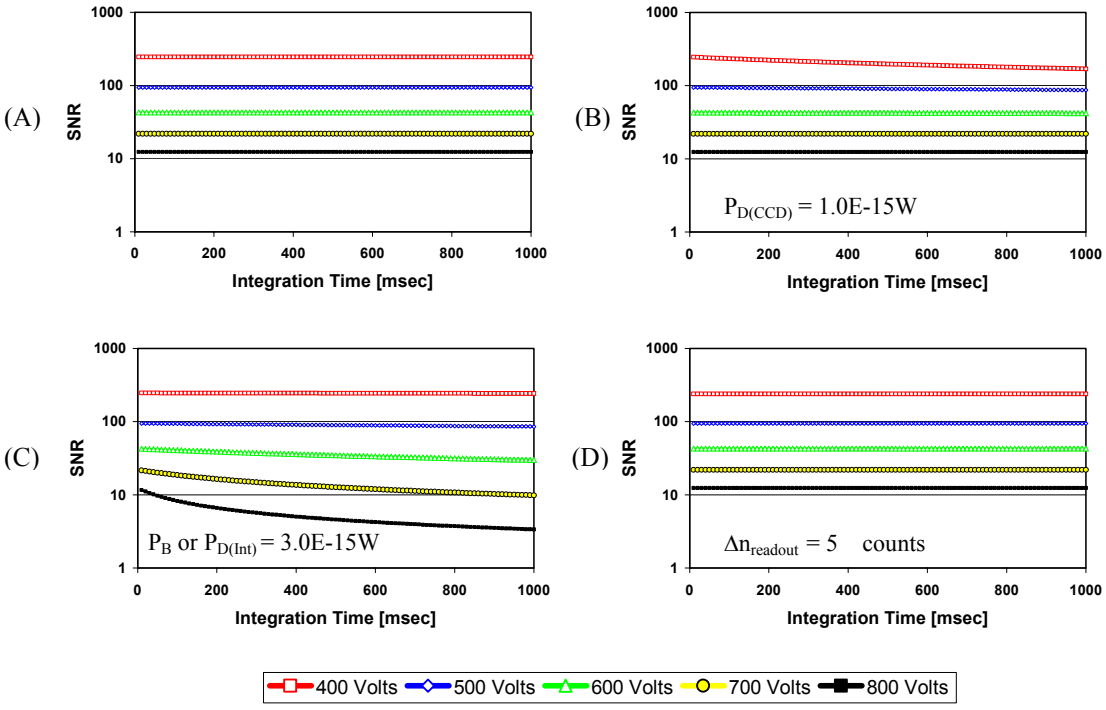

Figure 5.10. A sensitivity analysis is shown for the theoretical predictions of SNR versus integration time for constant integrated photons at several MCP gain voltages. Plot (A) shows the result of signal photon noise and excess MCP noise only. The other plots add noise in the proportions noted in the plots.

of the first noise term in the denominator of Equation 5.31 is responsible for the drop in SNR with integration time, as at higher integration times, fewer signal photons are required to achieve the 3000 counts. Plot (D) shows essentially no effect on the SNR for 5 counts of readout noise. Keep in mind, however, that for the type of image we are acquiring, there will be a large range in signal photons for different detector fibers. At

low signal counts, the readout noise will always limit SNR performance. As before, there is no dependence on the integration time, as the readout noise has no such dependence.

5.3 Summary

The most comprehensive treatment of ICCD noise to date was developed and presented in the context of a clinical breast imaging time-domain DOT system. This noise model can be used to better understand tradeoffs, requirements and limitations of using this technology as an effective tool in locating and identifying breast lesions. The noise model was used to explore the effect of various noise contributions on the SNR for developing insight into the noise character of measured data that will be presented in Chapter 6.

Chapter 5 References

1. M. A. Sartor, "Characterization and modeling of microchannel plate intensified CCD SNR variations with image size," SPIE Vol. **1655** Electron Tubes and Image Intensifiers, 74-84 (1992).
2. K. McCammon, K. Hagans, and A. Hankla, "Noise performance of microchannel plate imaging systems," SPIE Vol. **1346** Ultrahigh- and High-Speed Photography, Vidoagraphy, Photonics, and Velocimetry '90 398-403 (1990).
3. R. W. Boyd, Radiometry and the Detection of Optical Radiation, John Wiley & Sons, New York, 1983.
4. R. H. Kingston, Detection of Optical and Infrared Radiation, Springer-Verlag, New York, 1978.
5. R. J. Keyes, Optical and Infrared Detectors, Springer-Verlag, New York, 1977.
6. P. A. Tipler, Physics, Worth Publishers, Inc., New York, 1976.